Atmos. Chem. Phys. Discuss., 14, 23161–23200, 2014
www.atmos-chem-phys-discuss.net/14/23161/2014/
doi:10.5194/acpd-14-23161-2014

Atmospheric Chemistry and Physics Discussions

CCN activation of fumed silica aerosols mixed with soluble pollutants

M. Dalirian[1], H. Keskinen[2], L. Ahlm[1], A. Ylisirniö[2], S. Romakkaniemi[2,4], A. Laaksonen[2,3], A. Virtanen[2], and I. Riipinen[1]

[1]Department of Applied Environmental Science (ITM) and the Bolin Centre for Climate research, Stockholm University, Stockholm, Sweden
[2]Department of Applied Physics, University of Eastern Finland, Kuopio, Finland
[3]Finnish Meteorological Institute, Helsinki, Finland
[4]Finnish Meteorological Institute, Kuopio, Finland

Received: 13 June 2014 – Accepted: 20 August 2014 – Published: 8 September 2014

Correspondence to: M. Dalirian (maryam.dalirian@itm.su.se)

Published by Copernicus Publications on behalf of the European Geosciences Union.

Abstract

Particle-water interactions of completely soluble or insoluble particles are fairly well understood but less is known of aerosols consisting of mixtures of soluble and insoluble components. In this study, laboratory measurements were performed to investigate cloud condensation nuclei (CCN) activity of silica particles coated with ammonium sulphate (a salt), sucrose (a sugar) and bovine serum albumin known as BSA (a protein). In addition, the agglomerated structure of the silica particles was investigated by estimating the surface equivalent diameter based on measurements with a Differential Mobility Analyzer (DMA) and an Aerosol Particle Mass Analyzer (APM). By using the surface equivalent diameter the non-sphericity of the particles containing silica was accounted for when estimating CCN activation. Furthermore, characterizing critical supersaturations of particles consisting of pure soluble on insoluble compounds using existing frameworks showed that the CCN activation of single component particles was in good agreement with Köhler and adsorption theory based models when the agglomerated structure was accounted for. For mixed particles the CCN activation was governed by the soluble components, and the soluble fraction varied considerably with particle size for our wet-generated aerosols. Our results confirm the hypothesis that knowing the soluble fraction is the key parameter needed for describing the CCN activation of mixed aerosols, and highlight the importance of controlled coating techniques for acquiring a detailed understanding of the CCN activation of atmospheric insoluble particles mixed with soluble pollutants.

1 Introduction

The atmosphere of the Earth is composed of gases and suspended liquid and solid aerosol particles of different size, shape, and chemical composition. Atmospheric aerosols have several important impacts on the environment. First, at high concentrations in urban areas, they are a health hazard to the respiratory system causing

ACPD
14, 23161–23200, 2014

millions of premature deaths every year (Jacob, 1999; Mackay and Mensah, 2004; Pope III and Dockery, 2006; Pope III et al., 2009; Tranfield and Walker, 2012). Second, they scatter and absorb solar and thermal radiation and thereby directly influence the heat balance of the Earth and thus the climate (Twomy, 1974; McCormick and Ludwig, 1976; Jacob, 1999; Haywood and Boucher, 2000; Ramanathan et al., 2001; Lohmann and Feichter, 2005). Third, they act as cloud condensation nuclei (CCN) and ice nuclei (IN). Hence, they alter the microphysical properties of clouds and thereby indirectly affect the climate (Twomey, 1974; Twomey et al., 1984; Albrecht, 1989; Jacob, 1999; Haywood and Boucher, 2000; Lohmann and Feichter, 2005; Mcfiggans et al., 2006). Fourth, atmospheric surface and condensed-phase chemistry can occur in the aerosol phase (Jacob, 1999).

Aerosol–cloud interactions represent the largest uncertainty in predictions of the future climate (Carslaw et al., 2013; IPCC, 2013; Lee et al., 2013). To reduce this uncertainty we need to improve our understanding of the activation of aerosol particles to cloud droplets. In general, the ability of aerosol particles to act as CCN depends on their composition, size and structure (Kumar et al., 2011a). Besides soluble aerosol particles, insoluble particles like soot, mineral dust, and silica can act as CCN – particularly if they are coated with hygroscopic material (Kumar et al., 2009).

During atmospheric transport and aging, originally insoluble particles may acquire soluble species like $(NH_4)_2SO_4$ (ammonium sulphate) on their surfaces (Levin et al., 1996). In such cases, the threshold supersaturation of cloud droplet activation substantially decreases when water adsorbs onto the slightly soluble particles giving rise to the process of adsorption activation (Saathoff et al., 2003; Hings et al., 2008). Thus, the presence of soluble species on insoluble particle surfaces can enhance water–particle interactions and CCN activity of the particles. Several recent studies have focused on the CCN activation of insoluble and mixed soluble–insoluble particles, leading to the development of new theoretical frameworks for describing the relevant phenomena. The developed theories are often based on multilayer adsorption models and account for the curvature effects of the particles. One of these theories introduced by Sorjamaa

ACPD
14, 23161–23200, 2014

and Laaksonen (2007) combined FHH (Frenkel, Halsey and Hill) adsorption isotherms and traditional Köhler theory to describe the equilibrium growth of insoluble particles. Sorjamaa and Laaksonen (2007) showed that adsorption could help wettable insoluble compounds to activate in the atmosphere. Thereafter, Kumar et al. (2009) developed a cloud droplet formation parameterization where the CCN constitute an external mixture of soluble aerosol, that follows Köhler theory, and insoluble aerosol, that follows FHH adsorption activation theory (FHH-AT). They tested the new parameterization by comparing it to a numerical cloud model and found a good agreement between the parameterization and the model. Later Kumar et al. (2011a) reported laboratory measurements of CCN activity and droplet activation kinetics of aerosols dry generated from clays, calcite, quartz, silica and desert soil samples. They used FHH adsorption activation theory for describing fresh dust CCN activity and found that the adsorption activation theory describes fresh dust CCN activity better than Köhler theory. Afterward, Kumar et al. (2011b) studied particle size distributions, CCN activity, and droplet activation kinetics of wet generated aerosols from mineral particles and introduced a new framework of CCN activation of dust containing a soluble salt fraction, based on a combination of the traditional Köhler and FHH adsorption theories. Henning et al. (2010) on the other hand, studied agglomerated soot particles coated with levoglucosan and ammonium sulphate, and concluded that traditional Köhler theory was sufficient to describe the CCN activation of these mixed particles – as long as the amount of soluble material in the particles was known (see also Stratmann et al., 2010). Despite these pioneering studies, CCN activation measurements of partly insoluble particles containing a soluble fraction are still scarce.

Combustion processes result in emissions of different types of anthropogenic nanoparticles. Flame-made (fumed) silica (SiO_2) particles, mainly produced in flame reactors, are among these kind of particle types (Scheckman et al., 2009). Recently, fumed silica particles have been taken into consideration due to their industrial importance (Scheckman et al., 2009; Keskinen et al., 2011). In this study we use fumed silica particles as an experimental model to investigate the CCN activation of the insoluble

ACPD
14, 23161–23200, 2014

and partly soluble particles and the applicability of the current theoretical frameworks developed to describe this phenomenon. Furthermore, since the presented theories generally assume that the insoluble particles are spherical, the agglomerated structure of the silica particles could cause uncertainties in the CCN activation parameterizations. Taking into account the shape characterization of aggregated silica particles may overcome these uncertainties. Different studies have recently focused on parameterizing the structure of aggregated particles, especially silica agglomerates (Fuchs, 1964; DeCarlo et al., 2004; Virtanen et al., 2004; Biskos et al., 2006; Scheckman et al., 2009).

The main aims of this study are: (1) measuring the CCN activity of pure and mixed soluble–insoluble particles, (2) analysing and comparing the experimental results with theoretical calculations using the existing frameworks and (3) connecting the mass analysis and shape characterization of agglomerated silica particles to the existing theoretical frameworks to gain a better understanding of the structure effects of these particles. Laboratory measurements on the particle size distribution, mass, morphology and CCN activation of insoluble fumed silica mixed with different amounts of soluble materials were conducted. Furthermore, the experimental CCN activity results were compared to theoretical calculations using the framework introduced by Kumar et al. (2011b), and distribution of soluble material on wet-generated particle populations is discussed.

2 Experimental setup

Pure soluble or insoluble and mixed soluble–insoluble particles were generated and analysed in this study. The investigated mixed particles consisted of fumed silica (Degussa, Aerosil-90) as the insoluble part and three different hygroscopic components as the soluble part. The first hygroscopic component was ammonium sulphate which is a water-soluble inorganic salt with high hygroscopicity (Table 1); the second one was sucrose which is a sugar, i.e. a water-soluble organic; the third one was bovine

ACPD
14, 23161–23200, 2014

serum albumin (BSA) which is a large water-soluble protein with molecular dimensions of approximately 4 nm × 4 nm × 14 nm (Sugio et al., 1999; Jeyachandran et al., 2010). The SiO_2 used in the experiments was hydrophilic fumed silica, with a specific surface area of 90 $m^2\,g^{-1}$ and purity of ≥ 99.8 % from Evonik Industries. Ammonium sulphate and BSA were purchased from Sigma–Aldrich, and sucrose was purchased from VWR International BVBA. All chemicals had purities higher than 99 %.

Figure 1 shows a schematic of the experimental setup used in this study. Pure silica and pure soluble particles as well as mixed particles made of silica and soluble species were produced using the atomization-drying method described in Keskinen et al. (2011). Particles were generated by an aerosol generator (Model 3076, TSI Inc., USA) after dissolving materials in de-ionized water. The solute content in the water suspension was 0.06 wt%. For mixed particles, the ratios of soluble components to silica were 1 : 19, 1 : 9 and 1 : 3, implying that the fractions of soluble species were expected to be 5 %, 10 % and 25 % of total particulate mass in the atomized solution. We use the term solution, despite the fact that the insoluble silica particles were suspended in the water (instead of dissolved).

After the particles had been produced they were fed into a diffusion drier (Fig. 1) consisting of a porous tube surrounded by silica gel (Rotronic AG, model HC2-C04), resulting in a relative humidity (RH) below 5 % and they were neutralized using a charge neutralizer. Thereafter particle number size distributions were measured using a Scanning Mobility Particle Sizer (SMPS). The SMPS system was composed of an electrostatic classifier, which included a Differential Mobility Analyzer (DMA) (Model 3071; TSI, Inc.) to bin the particles according to electrical mobility, and an ultrafine Condensation Particle Counter (CPC Model 3025; TSI, Inc.) to count the size-binned particles exiting the DMA.

Simultaneously, size-resolved CCN activity of the generated particles was measured using a CCN counter (CCNc; Droplet Measurement Technologies Inc.) Roberts and Nenes, 2005) (Fig. 1). Before entering the CCNc, particles were size classified by a DMA, of the same model as the DMA used in the SMPS. The CCNc operates by

ACPD
14, 23161–23200, 2014

supersaturating sample air to the point where the CCN become detectable particles. The supersaturation can be varied between 0.1 % and 1.5 %. The total number concentration of the particles entering the CCNc was measured by a CPC (Model 3772; TSI, Inc.) and the number of activated droplets was counted by an Optical Particle Counter (OPC) over 20 size bins in the diameter range from 0.75 to 10 µm.

The effect of the silica particle morphology on activation was investigated by measuring the mass of size classified particles by Aerosol Particle Mass Analyzer (APM) (model APM-3600; Kanomax Inc.) (Fig. 1) (McMurry et al., 2002; Park et al., 2003a, b). The APM provides a direct relationship between applied voltage, rotation speed, and particle mass (Liu et al., 2012). Therefore, by measuring the outlet number concentration of the APM corresponding to different applied voltages of the instrument, it was possible to measure the mass distribution of the size selected particles. For each APM voltage, the downstream number concentration was measured by a CPC (Model 3772; TSI, Inc.) (Fig. 1). From the voltage corresponding to the highest concentration the average particle mass was calculated using the following equation (McMurry et al., 2002; Park et al., 2003b):

$$m = \frac{qV}{r^2\omega^2 \ln(r_2/r_1)} \quad (1)$$

where m is the particle mass, ω is the APM angular speed, V is the applied voltage, q is the particle charge, and r_1, r_2 and r are the inner, outer and rotating radius of the instrument, respectively.

3 Theoretical frameworks

3.1 Non-sphericity of particles

Two parameters, dynamic shape factor (χ) and fractal dimension (D_f), have been widely used to characterize non-sphericity of aerosol particles. Dynamic shape factor is de-

ACPD
14, 23161–23200, 2014

fined as the ratio of the drag force on the agglomerated particles to the drag force on the volume equivalent (or in some studies mass equivalent) spherical particles (DeCarlo et al., 2004; Fuchs, 1964; Kelly and McMurry, 1992; Kumar et al., 2011b), and fractal dimension is the coordination number in the aggregate and links properties like surface area of a particle to the scale of the measurements (Hinds, 1999; Ibaseta and Biscans, 2010). These parameters are applicable to quantify the morphology of agglomorated particles.

The shape factor is defined as Kelly and McMurry (1992):

$$\chi = \frac{C(d_{me})}{C(d_b)} \cdot \left(\frac{\rho_p}{\rho_e}\right)^{1/3} \quad (2)$$

where d_b and d_{me} are mobility diameter and mass equivalent diameter, $C(d_b)$ and $C(d_{me})$ are the corresponding Cunningham slip correction factors, ρ_p is particle bulk density and ρ_e is particle effective density. The effective density of particles (ρ_e) was estimated using the following equation (Kelly and McMurry, 1992; Park et al., 2003a; Virtanen et al., 2004; Liu et al., 2012):

$$\rho_e = m/\left(\pi d_b^3/6\right), \quad (3)$$

where m is the mass of the particles determined by using APM (Eq. 1). The mass equivalent diameter (d_{me}) was calculated by the following equation (Kelly and McMurry, 1992):

$$d_{me} = \left(\frac{6\,m}{\pi\rho_p}\right)^{1/3} \quad (4)$$

where ρ_p is the material density of the silica particle (see Table 1)

Slip correction factors are given by (Kulkarni et al., 2011; Kumar et al., 2011b):

$$C(d_i) = 1 + \frac{2\lambda}{d_i}\left(1.142 + 0.558\exp\left(-0.999\frac{d_i}{2\lambda}\right)\right) \quad (5)$$

ACPD
14, 23161–23200, 2014

where λ is the mean free path of the gas molecules and d_i corresponds to either of d_{me} or d_b.

The fractal dimension of the particles was determined using the scaling law for effective density vs. mobility diameter (Skillas et al., 1998, 1999; Virtanen et al., 2004):

$$\rho_e \propto d_b^{(D_f-3)} \tag{6}$$

After estimating the shape factor of the aggregates, the volume equivalent diameter (d_{Ve}) and surface equivalent diameter (d_{se}) of the particles were calculated using the following relations (DeCarlo et al., 2004; Kumar et al., 2011a):

$$\frac{d_{Ve}}{C(d_{Ve})} = \frac{d_b}{\chi \cdot C(d_b)} \tag{7}$$

$$d_{se} = \frac{3\chi d_{Ve} - d_b}{2} \tag{8}$$

The effect of non-sphericity on CCN activation was accounted for by using the surface equivalent diameter (d_{se}), instead of mobility diameter (d_b), for pure and mixed silica particles. From here on we will thus use d_{dry} to denote the surface equivalent diameter.

3.2 CCN activation of soluble particles

κ-Köhler theory (Petters and Kreidenweis, 2007) was used to estimate the critical supersaturation of pure ammonium sulphate, sucrose and BSA particles. The saturation ratio (S) is expressed as:

$$S = \frac{d_p^3 - d_{dry}^3}{d_p^3 - d_{dry}^3(1-\kappa)} \exp\left(\frac{4\sigma_w M_w}{RT\rho_w d_p}\right) \tag{9}$$

where σ_w is the water surface tension, ρ_w is the water density, M_w is the molar mass of water, R is the universal gas constant, T is the temperature, d_{dry} is the dry particle

ACPD
14, 23161–23200, 2014

diameter, d_p is the droplet diameter and κ is the hygroscopicity parameter of soluble particles.

The supersaturation (s) is equal to ($S - 1$) and is expressed as a percentage. The maximum value of the supersaturation is called critical supersaturation (s_c) – similar definition naturally holding for critical saturation ratio S_c as well. Thus, at the critical point:

$$\left.\frac{ds}{dd_p}\right|_{d_p=d_c} = 0 \tag{10}$$

where d_c is called the critical diameter. The κ values for pure soluble particles were extracted from previous studies or, in the case of BSA, derived by applying the following relation introduced by Petters and Kreidenweis (2007) to our observations of the critical supersaturations of the pure soluble particles:

$$\kappa = \frac{4A^3}{27 d_{dry} \ln^2 S_c} \tag{11}$$

where S_c is the saturation ratio at the critical point, $A = \frac{4\sigma M_w}{RT\rho_w}$, $\sigma = 0.072\,\mathrm{J\,m^{-2}}$, $T = 298.15\,\mathrm{K}$, $M_w = 0.018\,\mathrm{kg\,mol^{-1}}$ and $\rho_w = 1000\,\mathrm{kg\,m^{-3}}$.

3.3 CCN activation of insoluble silica

The critical supersaturation of pure silica particles was calculated using FHH adsorption theory (Sorjamaa and Laaksonen, 2007; Kumar et al., 2009, 2011a). In this case the relationship between water supersaturation s and particle size can be expressed as:

$$s = \frac{4\sigma_w M_w}{RT\rho_w d_p} - A_{FHH}\left(\frac{d_p - d_{dry}}{2d_{H_2O}}\right)^{-B_{FHH}} \tag{12}$$

ACPD
14, 23161–23200, 2014

where d_{H_2O}(= 2.75 Å) is the diameter of the water molecule, and A_{FHH} and B_{FHH} are the FHH adsorption isotherm parameters. The first and second terms on the right hand side of Eq. (12) correspond to the contributions from the Kelvin and adsorption effects, respectively.

In the literature, different values of the parameters A_{FHH} and B_{FHH} for silica particles have been reported. Kumar et al. (2011a) obtained the values 2.95 and 1.36 for A_{FHH} and B_{FHH} of quartz silica, respectively, and Keskinen et al. (2011) assigned values of 4.82 and 2.16 for A and B for non-agglomerated fumed silica particles (Degussa, Aerosil-300) with the diameter of 8 and 10 nm.

3.4 CCN activation of mixed soluble and insoluble particles

Kumar et al. (2011b) used adsorption activation theory assuming that the particles are spheres and presented a shell-and-core model with the core consisting of insoluble dust, and the shell consisting of a layer of soluble salt. They presumed that the soluble part coats the insoluble part and introduced the following relation between water supersaturation, particle size and composition:

$$s = \frac{4\sigma_w M_w}{RT\rho_w d_p} - \frac{\varepsilon_s d_{dry}^3 \kappa}{\left(d_p^3 - \varepsilon_i d_{dry}^3\right)} - A_{FHH}\left(\frac{d_p - \varepsilon_i^{1/3} d_{dry}}{2d_{H_2O}}\right)^{-B_{FHH}} \quad (13)$$

where ε_i an $d\varepsilon = 1-\varepsilon$ are the insoluble and soluble volume fractions in the dry particles and κ is the hygroscopicity parameter of the soluble part. A_{FHH} and B_{FHH} are the FHH adsorption isotherm parameters of the insoluble part.

To estimate the average insoluble volume fractions of the mixed particles, the following relation was used:

$$\varepsilon_i = \frac{m_i/\rho_i}{m_i/\rho_i + m_s/\rho_s} \quad (14)$$

ACPD
14, 23161–23200, 2014

where m_i and m_s are the insoluble and soluble mass fractions in the total mixed aerosol population, and ρ_i and ρ_s are the densities of the insoluble and soluble parts, respectively. The bulk densities of the used components are listed in Table 1.

4 Results and discussion

4.1 Particle size distributions

The SMPS measurements yielded the average number size distributions for silica particles mixed with $(NH_4)_2SO_4$, sucrose and BSA (Fig. 2). Figure 2a displays average number size distributions for particles made of pure fumed silica, pure $(NH_4)_2SO_4$ and particles made of silica and different amounts of $(NH_4)_2SO_4$. As is evident in the figure, size distributions of particles generated from pure silica or pure $(NH_4)_2SO_4$ are unimodal while size distributions of particles generated from the silica-$(NH_4)_2SO_4$ mixtures are bimodal. The mean mobility diameter is ~ 30 nm for the pure $(NH_4)_2SO_4$ particles, and approximately 150 nm for the pure silica particles. The first mode of the bimodal size distributions, associated with particles generated from the aqueous bulk mixtures, is centered at a diameter of less than 30 nm. The second mode, with lower number concentration, is centered at approximately 150 nm. Figure 2b shows the average number size distributions of particles made of sucrose and silica. Particles made of pure sucrose have a mean diameter of approximately 50 nm. Size distributions associated with particles generated from the silica-sucrose mixtures are bimodal (Fig. 2b); the first mode centered at a diameter of less than 50 nm and the second mode centered at a diameter of about 150 nm. Similarly, Fig. 2c shows the average SMPS number size distributions of particles made of silica and BSA. These data are comparable with previous two measurements in Fig. 2a and b. The particles made of the large BSA protein have a mean diameter of about 75 nm. The mode associated with particles made of a mixture of BSA and silica is centered at about 150 nm.

ACPD
14, 23161–23200, 2014

In the case of mixed aerosols, the particles in the first mode of the bimodal size distributions are likely pure soluble particles, while the second mode of the bimodal distribution curves represents silica particles mixed with soluble species. Hence, when analysing the activation behaviour of mixed particles we omitted the CCNc data of the smallest particles by subtracting their contribution from the CCN numbers and restricted our analysis to particle sizes larger than 100 nm.

In order to estimate the average soluble volume (mass) fractions in the mixed particles, we calculated the amount of soluble material in the first mode of the particle size distributions and subtracted it from the total soluble mass. In this regard, we fitted log-normal distribution curves to the number size distributions associated with particles from the mixtures and estimated the volume and mass distributions related to each particle number size distribution. Hereupon, it was possible to estimate the fraction of total soluble mass remaining in the first mode of the bimodal size distributions for each mixture, and the fraction of total soluble mass which was mixed with silica (Table 2). By multiplying this fraction with the soluble mass fraction in the bulk mixture we gained an estimate of the real average soluble mass fraction in the mixed/coated particles excluding the portion of the pure soluble particles. As is evident from Table 2, the mass losses of solubles from the first mode are small, and 87–100 % of the total soluble masses were mixed with silica particles.

4.2 Mass analysis and size characterization of silica particles

Since fumed silica particles are agglomerates, mass analysis of the pure silica particles could help us to get a better understanding of their shape. Therefore, we estimated the effective density and shape factor for these particles. As an example, Fig. 3a shows the observed average number concentrations of 100 nm size-selected silica particles (by DMA) for different APM voltages. A log-normal distribution was fitted to provide the voltage value corresponding to the peak of the distribution. After determining the mass of size selected particles using Eq. (1), the effective density of silica particle was estimated (Eq. 3). The APM measurements were performed for two different rotation

ACPD
14, 23161–23200, 2014

speeds of the APM (3000 and 5000 rpm). The achieved effective particle densities using these two rotation speeds are presented in Fig. 3b. There is only a small difference in effective density between the two different speeds, giving confidence in the results. Afterward, the fractal dimension of the silica particles was estimated using the slopes of the curves in Fig. 3b and Eq. (6). The slope values, 2.54 and 2.55, were fitted respectively for D_f of the silica particles in 3000 and 5000 rpm speed of the APM instrument. Fitted D_f values are close to the value ($D_f = 2.57$) reported by Keskinen et al. (2011) and Ibaseta and Biscans (2010) ($D_f = 2$ to 2.5) for fumed silica (Degussa, Aerosil-300 and -200, respectively). Figure 3c displays the dynamic shape factor of silica particles for different mobility diameters. The shape factor of the silica particles increases by increasing mobility diameter, which indicates that irregularities in particle shape or internal voids within the particles increase with increasing particle diameter (Kelly and McMurry, 1992). By using the derived shape factors the surface equivalent diameter corresponding to different mobility diameters of silica particles (using Eq. 8) could be estimated (Fig. 3d). As expected, because of the void spaces inside the silica agglomerates, the surface equivalent diameter for silica particles is larger than its corresponding mobility diameter. The surface equivalent diameter was then used in all the theoretical calculations to represent the physical size of the particles in Eqs. (12) and (13).

4.3 CCN activation results

Before analysing the CCN activity of the generated particles, all the activation curves were charge-corrected using the procedure introduced by Moore et al. (2010). Furthermore, the contributions of the smaller completely soluble particle mode (see Fig. 2) were subtracted from the CCN concentrations. The ratio of the corrected CCN and CN (Condensation Nuclei, measured by CPC) time series thus determines the activated fraction (also referred to as activation ratio) of the specified particles (Kumar et al., 2011a).

ACPD
14, 23161–23200, 2014

4.3.1 CCN behavior of pure components

Figure 4 shows the activation ratio dependence on supersaturation for 120 nm (mobility diameter) pure silica, BSA, sucrose and ammonium sulphate particles. A sigmoid curve was fitted to each set of activation ratio data. Critical supersaturation (s_c) is often associated with the supersaturation where 50 % of the particles are CCN activated – equivalent to a CCN/CN-ratio of 50 %, and we will follow this convention although the two are not necessarily equal when the CCN/CN curve is not a step function. As expected, $(NH_4)_2SO_4$ particles, which are the most hygroscopic particles investigated in this study (see κ values in Table 1), activated at lower supersaturations than was the case for sucrose, silica and BSA particles. The pure silica particles, which are insoluble and non-hygroscopic, exhibited the highest critical supersaturation of the investigated compounds (Fig. 4).

Figure 5 displays activation ratio against supersaturation for pure silica particles of different mobility diameters. As is evident from Fig. 5, the critical supersaturation decreases with increasing particle diameter. Experimentally and theoretically determined critical supersaturations of pure silica particles as a function of particle mobility diameter are shown in Fig. 6. Previously, the values for FHH adsorption parameters (Eqs. 10 and 12) of different types of silica have been determined by Kumar et al. (2011a) (quartz), and Keskinen et al. (2011) (Fumed silica, Aerosil-300). To compare our results (Fumed silica, Aerosil-90) of the pure silica activation to these studies, we fitted the FHH adsorption parameters for pure silica particles. A_{FHH} and B_{FHH} values of 2.5 and 1.9 explain our results on the activation diameter vs. critical supersaturation (Fig. 6), although the fits were difficult to constrain uniquely. The results indicate, however, that our results are better in line with the work of Keskinen et al. (2011) than Kumar et al. (2011a) – although the A_{FHH} and B_{FHH} values are close to those reported by Kumar et al. (2011a). This highlights the sensitivity of the fits to these values, reflecting the fact that our data set is not sufficient for constraining any physical or chemical phenomena behind these values. It must be pointed out that the quartz

ACPD
14, 23161–23200, 2014

silica (Kumar et al., 2009) is not as hydrophilic as fumed silica which probably affects the critical supersaturation. Furthermore, the FHH adsorption parameters in Keskinen et al. (2011) study were fitted for only 8 and 10 nm fumed silica particles which were most likely spherical and thus potentially not fully representative of the agglomerated particles that we used. Impurity of the silica could also affect the results even though the water conditions were as pure as possible in all studies. To conclude, the experimental results for s_c of pure silica particles were in good agreement with theoretical calculations using FHH adsorption isotherm and small deviations were only observed for larger diameters.

To estimate the critical supersaturations of pure soluble particles, κ-Köhler theory (Eqs. 9 and 10) was applied. Table 1 lists κ values of the soluble materials used in this study. The ability for ammonium sulphate particles to act as CCN has been widely studied (e.g. Garland, 1969; Kreidenweis et al., 2005; Hiranuma et al., 2011), and here we employed the previously-reported hygroscopicity (κ) values (Petters and Kreidenweis, 2007). The κ value for pure sucrose was extracted from Ruehl et al. (2010). For the pure BSA particles it was calculated based on Eq. (11) using the CCN activation results of pure BSA particles in this study. Theexperimentally and theoretically determined critical supersaturations for pure $(NH_4)_2SO_4$, BSA and sucrose particles are shown in Fig. 7. Indeed, κ-Köhler theory results were in good agreement with the experimentally determined critical supersaturations of pure soluble particles.

4.3.2 CCN behavior of the mixtures

Here we present the CCN activation results of co-synthesized silica particles mixed with $(NH_4)_2SO_4$, sucrose or BSA considering the determined total soluble fractions in the mixed particle population from Table 2.

The activation ratio curves were determined for different diameters of mixed particles and different ratios of soluble to insoluble materials. Figure 8 shows the activation ratio curves for 150 nm (mobility diameter) pure and mixed particles. Figure 8a shows the activation probabilities of mixed silica-$(NH_4)_2SO_4$ particles. The critical supersatu-

ACPD
14, 23161–23200, 2014

ration (corresponding to CCN/CN = 50 %) is higher for pure silica particles than for the particles with soluble material. Evidently, the pure $(NH_4)_2SO_4$ particles have the lowest critical supersaturation. Furthermore, the critical supersaturation decreases when the fraction of soluble material in the particles increases, and the CCN/CN curves are shallower (i.e. further from a step function) for the mixed as compared with the pure particles. The same behavior can be observed in Fig. 8b for 150 nm silica particles mixed with sucrose. Pure sucrose particles were activated at a supersaturation of 0.22 % which is comparable to previous studies of sucrose (e.g. Rosenorn et al., 2006). s_c decreases with increasing sucrose ratio in the mixed particles, similar to what was observed for ammonium sulphate in Fig. 8a. In the case of particles containing BSA, however, a different behavior was observed: s_c was higher for particles made of 5 % and 10 % BSA than for particles made of pure silica (Fig. 8c). The reason for this behavior is not clear but it is known that adsorption of BSA on silica can affect the structural properties of BSA. As was explained by Larsericsdotter et al. (2005), for soft proteins such as BSA the structural stability decreases when adsorption onto other materials occurs. On the other hand, the BSA can also affect the agglomerate structure of the mixed particles – for instance through more compact agglomerates with increasing BSA concentrations (see e.g. Kiselev et al., 2010; Stratmann et al., 2010 for discussion on effects of coating on agglomerate compactness). However, it is also possible that this effect is solely due to different distribution of the soluble materials as a function of particle size for the different bulk solution compositions, which is discussed in detail below.

To estimate the soluble mass fractions (ω_ss) in the coated/mixed particles required for the application of Eq. (13), the total amount of soluble coating was first estimated by fitting log-normal size distributions to the observed size distributions (Sect. 4.1). The dashed lines in Fig. 9 show the theoretical critical supersaturations (using Eq. 13) of particles consisting of a mixture of silica and ammonium sulphate assuming soluble volume fractions (ε_ss) corresponding to these constant ω_ss (see Table 2 and the dashed lines of the insert in Fig. 9) with changing diameter. These theoretical values

ACPD
14, 23161–23200, 2014

of critical supersaturations are mostly lower than the observed critical supersaturations (stars), and the size-dependence of the critical supersaturation is not captured by the theory. We observed the same (although less pronounced) behavior for silica particles mixed with sucrose and BSA (Figs. 10 and 11). In all three cases, the observed critical supersaturations were higher than expected from the shell-core model by Kumar et al. (2011b) using constant soluble mass fractions. The calculations are very sensitive to the κ values and the deviation between experimental and estimated s_c for mixed particles increases with increasing hygroscopicity. The largest deviations were observed for particles mixed with $(NH_4)_2SO_4$, which is more hygroscopic ($\kappa = 0.61$) than the other compounds, and the smallest deviations were observed for silica particles mixed with BSA which has the lowest hygroscopicity ($\kappa = 0.01$). The adsorption term contribution to the critical supersaturation in Eq. (13) was generally minor: $< 0.72\,\%$ for silica$(NH_4)_2SO_4$, $< 3.8\,\%$ for silicasucrose and $< 7\,\%$ for silica + BSA of the total (kelvin + solubility + adsorption) contribution for all the studied compositions and supersaturations. The theoretical predictions were thus dominated by the Kelvin and solubility effects – similarly to the case of soot agglomerates studied by Henning et al. (2010).

The small contribution of the adsorption term to the theoretical predictions combined with the shallow activation ratio curves (see Fig. 8) suggest that the reason for the apparent discrepancy between the theoretical and the observed critical supersaturations is a non-constant distribution of the soluble material with varying particle size. This explanation seems particularly feasible taking into account the good agreement between the experiments and theory for the pure particles, and the fact that the particle generation method (atomization and drying of aqueous solutions) does not allow for controlling the ratio of soluble to insoluble materials at a given particle size – only for the overall aerosol population. To yield further insight into this, we estimated the distribution of the soluble material by fitting size-dependent ε_s distributions to the CCN/CN vs. s_c curves (e.g. Fig. 8) using Eq. (13) – thus assuming that all the mixed particles that activate at a given supersaturation interval contain a specific soluble volume (mass) fraction. It is

ACPD
14, 23161–23200, 2014

worthwhile to note that the ε_s determined this way correspond to the surface equivalent diameter (linked to the volume equivalent diameter through the effective density, see Sect. 3), and is thus not directly comparable to the mass fractions in the atomized solution.

The s_c (defined as the 50 % point in the CCN/CN curves) vs. mobility diameter results obtained through the fitting procedure are shown by the solid lines in Figs. 9–11, and the resulting soluble mass fractions ω_ss corresponding to the ε_ss fitted to the 50 % points in the CCN/CN curves as a function of particle size are shown as the solid lines in the inserts. The results suggest a very uneven distribution of the soluble material as a function of particle size: the small particles contain considerably higher fractions of soluble material than the larger ones, and the effect increases with the amount of soluble material. In the case of BSA, there even appears to be a large number of pure BSA particles present at the low end of the "mixed" size distribution governing the 50 % activation point.

While the size-dependent ω_s shown in Figs. 9–11 correspond to the points at which 50 % of the CN activate as CCN for a given particle diameter and supersaturation, the ω_s values vary even for a given particle size – as indicated by non-step function shape of the activation curves in Fig. 8. An example distribution of the soluble mass as deduced from the CCN/CN vs. s_c data (Fig. 8) using Eq. (13) is shown in Fig. 12 for the 150 nm mobility diameter mixed particles. The figure shows that for each mixture, there is an uneven distribution of soluble mass fraction in the particles of a given size (here 150 nm). In all cases, there are large amount of particles with very low soluble mass fractions (less than initial bulk solution) and the composition of the size-selected particles is not constant. Similar conclusions were drawn by Dusek et al. (2006) for soot particles coated by NaCl. When compared to the mass fractions in the atomized solution, it can be seen that only in the case of sucrose the distribution peaks at soluble mass fractions similar to the original solution, while the mixtures containing ammonium sulphate and BSA have widely varying compositions.

ACPD
14, 23161–23200, 2014

5 Summary and conclusions

In this study, the CCN activation of pure and mixed particles of silica and soluble compounds (AS, sucrose and BSA) was investigated. Furthermore, the morphology and effective density of silica particles were investigated based on APM measurements. In addition, size distributions of the sampled particles were measured using a SMPS. Then non-sphericity of the particles was investigated by applying APM measurements and estimating dynamic shape factors and fractal dimensions of pure silica particles. By using these derived shape factors, the surface equivalent diameter corresponding to different mobility diameters of the silica particles, which was needed for the theoretical calculations, was estimated. The SMPS results showed that the particles generated from pure compounds resulted in unimodal size distributions, while the particles generated from mixtures were associated with bimodal size distributions. The first peak of the bimodal size distribution indicated that also the mixture generated some pure soluble particles. The size distributions allowed us to estimate the total soluble vs. insoluble mass fractions present in the mixed particle population.

CCN activity measurements were conducted in various supersaturations up to 1.5 %, and activation ratio curves were determined for the evaluated particles. Afterward, the experimental data were compared to theoretical values using adsorption theory (e.g. Sorjamaa and Laaksonen, 2007) for the pure silica particles, κ-Köhler-theory (Petters and Kreidenweis, 2007) for the pure soluble particles, and a shell and core model introduced by Kumar et al. (2011b) for the mixed particles. The CCN activation of pure soluble and insoluble particles was in good agreement with κ-Köhler theory and adsorption theory. For mixed particles, however, the observed critical supersaturations were higher than those expected from the shell and core model, if constant soluble and insoluble mass fractions were assumed for the whole mixed particle population. This indicates that the particles were less hygroscopic than expected, indicating an uneven distribution of the soluble material in the aerosol size distribution. As the calculations were governed by the soluble mass (volume) fraction in the particles instead

ACPD
14, 23161–23200, 2014

of adsorption effects, we could use the experimental critical supersaturations to estimate size-dependent distribution of the soluble material in the mixed particles. For particles > 150 nm in mobility diameter the soluble fractions were smaller and for particles < 150 nm mostly larger than in the total mixed particle population – indicating that the soluble material preferentially accumulated to particles < 150 nm, independent of the exact identity of the soluble species. If the uneven distribution of the soluble material was accounted for, the framework by Kumar et al. (2011b) could be successfully used to describe the CCN activation of insoluble particles mixed with soluble pollutants.

Our results indicate that knowing the fraction of soluble material (instead of the adsorption properties of the surfaces) is the key prerequisite for describing the CCN activation of silica mixed with soluble pollutants – at least for the relatively large soluble fractions studied here. Our mixed particles consistent of varying soluble fractions, thus probably representing an aerosol population with various degrees of aging in the atmosphere. Furthermore, our results indicate that well-defined descriptions of the coating processes are crucial for elucidating the phenomena governing the CCN activation of insoluble particles mixed with soluble compounds.

Acknowledgements. Financial support from the Nordic Centre of Excellence CRAICC (Cryosphere-atmosphere interactions in a changing Arctic climate), Vetenskaprådet (grant n:o 2011-5120), Academy of Finland (272041, 259005) and the European Research Council (StG n:o 27877 ATMOGAIN and 335478 QAPPA) is gratefully acknowledged.

References

Albrecht, B. A.: Aerosols, cloud microphysics, and fractional cloudiness, Science, 245, 1228–1230, 1989.

Biskos, G., Russell, L. M., Buseck, P. R., and Martin, S. T.: Nanosize effect on the hygroscopic growth factor of aerosol particles, Geophys. Res. Lett., 33, L07801, doi:10.1029/2005GL025199, 2006.

Carslaw, K. S., Lee, L. A., Reddington, C. L., Pringle, K. J., Rap, A., Forster, P. M., Mann, G. W., Spracklen, D. V, Woodhouse, M. T., Regayre, L. A., and Pierce, J. R.:

ACPD
14, 23161–23200, 2014

Large contribution of natural aerosols to uncertainty in indirect forcing, Nature, 503, 67–71, doi:10.1038/nature12674, 2013.
DeCarlo, P. F., Slowik, J. G., Worsnop, D. R., Davidovits, P., and Jimenez, J. L.: Particle morphology and density characterization by combined mobility and aerodynamic diameter measurements, Part 1: theory, Aerosol Sci. Tech., 38, 1185–1205, doi:10.1080/027868290903907, 2004.
Dusek, U., Reischl, G. P., and Hitzenberger, R.: CCN activation of pure and coated carbon black particles, Environ. Sci. Technol., 40, 1223–1230, 2006.
Fuchs, N. A.: The Mechanics of Aerosols, Pergamon Press, London, 1964.
Garland, J. A.: Condensation on ammonium sulphate paticles and its effect on visibility, Atmos. Environ., 3, 347–354, 1969.
Grayson, M. (Ed.): Encyclopedia of Glass, Ceramics and Cement, John Wiley & Sons, Inc., New York, 1985.
Haynes, W. M., Bruno, T. J., and Lide, D. R. (Eds.): CRC Handbook of Chemistry and Physics, 94th edn., CRC Press, available at: http://www.hbcpnetbase.com/, last access: 19 July 2013.
Haywood, J. and Boucher, O.: Estimates of the direct and indirect radiative forcing due to tropospheric aerosols: a review, Rev. Geophys., 38, 513–543, 2000.
Henning, S., Wex, H., Hennig, T., Kiselev, A., Snider, J. R., Rose, D., Dusek, U., Frank, G. P., Pöschl, U., Kristensson, A., Bilde, M., Tillmann, R., Kiendler-Scharr, A., Mentel, T. F., Walter, S., Schneider, J., Wennrich, C., and Stratmann, F.: Soluble mass, hygroscopic growth, and droplet activation of coated soot particles during LACIS Experiment in November (LExNo), J. Geophys. Res., 115, D11206, doi:10.1029/2009JD012626, 2010.
Hinds, W. C.: Aerosol Technology: Properties, Behavior, and Measurement of Airborne Particles, 2nd Edn., John Wiley & Sons Inc., New York, 1999.
Hings, S. S., Wrobel, W. C., Cross, E. S., Worsnop, D. R., Davidovits, P., and Onasch, T. B.: CCN activation experiments with adipic acid: effect of particle phase and adipic acid coatings on soluble and insoluble particles, Atmos. Chem. Phys., 8, 3735–3748, doi:10.5194/acp-8-3735-2008, 2008.
Hiranuma, N., Kohn, M., Pekour, M. S., Nelson, D. A., Shilling, J. E., and Cziczo, D. J.: Droplet activation, separation, and compositional analysis: laboratory studies and atmospheric measurements, Atmos. Meas. Tech., 4, 2333–2343, doi:10.5194/amt-4-2333-2011, 2011.

ACPD
14, 23161–23200, 2014

Ibaseta, N. and Biscans, B.: Fractal dimension of fumed silica: comparison of light scattering and electron microscope methods, Powder Technol., 203, 206–210, doi:10.1016/j.powtec.2010.05.010, 2010.
IPCC: (Intergovernmental Panel on Climate Change): Climate Change 2013, The Physical Science Basis, Cambridge University Press, Cambridge, 2013.
Jacob, D. J.: Introduction to atmospheric chemistry, Princeton University Press, Princeton, available at: http://acmg.seas.harvard.edu/publications/jacobbook/index.html (last access: 8 September 2014), 1999.
Jeyachandran, Y. L., Mielczarski, J. A., Mielczarski, E., and Rai, B.: Efficiency of blocking of non-specific interaction of different proteins by BSA adsorbed on hydrophobic and hydrophilic surfaces., J. Colloid Interface Sci., 341, 136–142, doi:10.1016/j.jcis.2009.09.007, 2010.
Kelly, W. P. and McMurry, P.: Measurement of particle density by inertial classification of Differential Mobility Analyzer-generated monodisperse aerosols, Aerosol Sci. Tech., 17, 199–212, 1992.
Keskinen, H., Romakkaniemi, S., Jaatinen, A., Miettinen, P., Saukko, E., Jorma, J., Mäkelä, J. M., Virtanen, A., Smith, J. N., and Laaksonen, A.: On-line characterization of morphology and water adsorption on fumed silica nanoparticles, Aerosol Sci. Tech., 45, 1441–1447, doi:10.1080/02786826.2011.597459, 2011.
Kiselev, A., Wennrich, C., Stratmann, F., Wex, H., Henning, S., Mentel, T. F., Kiendler-Scharr, A., Schneider, J., Walter, S., and Lieberwirth, I.: Morphological characterization of soot aerosol particles during LACIS Experiment in November (LExNo), J. Geophys. Res., 115, D11204, doi:10.1029/2009JD012635, 2010.
Kreidenweis, S. M., Koehler, K., DeMott, P. J., Prenni, A. J., Carrico, C., and Ervens, B.: Water activity and activation diameters from hygroscopicity data - Part I: Theory and application to inorganic salts, Atmos. Chem. Phys., 5, 1357–1370, doi:10.5194/acp-5-1357-2005, 2005.
Kulkarni, P., Baron, P. A., Willeke, K. (Ed.): Aerosol measurement: principles, techniques, and applications, 3rd edn., John Wiley & Sons, Inc., Hoboken, New Jersey, 2011.
Kumar, P., Sokolik, I. N., and Nenes, A.: Parameterization of cloud droplet formation for global and regional models: including adsorption activation from insoluble CCN, Atmos. Chem. Phys., 9, 2517–2532, doi:10.5194/acp-9-2517-2009, 2009.
Kumar, P., Sokolik, I. N., and Nenes, A.: Measurements of cloud condensation nuclei activity and droplet activation kinetics of fresh unprocessed regional dust samples and minerals, Atmos. Chem. Phys., 11, 3527–3541, doi:10.5194/acp-11-3527-2011, 2011a.

ACPD
14, 23161–23200, 2014

Kumar, P., Sokolik, I. N., and Nenes, A.: Cloud condensation nuclei activity and droplet activation kinetics of wet processed regional dust samples and minerals, Atmos. Chem. Phys., 11, 8661–8676, doi:10.5194/acp-11-8661-2011, 2011b.

Larsericsdotter, H., Oscarsson, S., and Buijs, J.: Structure, stability, and orientation of BSA adsorbed to silica, J. Colloid Interf. Sci., 289, 26–35, doi:10.1016/j.jcis.2005.03.064, 2005.

Lee, L. A., Pringle, K. J., Reddington, C. L., Mann, G. W., Stier, P., Spracklen, D. V., Pierce, J. R., and Carslaw, K. S.: The magnitude and causes of uncertainty in global model simulations of cloud condensation nuclei, Atmos. Chem. Phys., 13, 8879–8914, doi:10.5194/acp-13-8879-2013, 2013.

Levin, E. L., Spector, P. E., Menon, S., Narayanan, L., and Cannon-Bowers, J. A.: The effects of desert particles coated with sulfate on rain formation in the eastern Mediterranean, Hum. Perform., 9, 1511–1523, 1996.

Liu, Q., Ma, X., and Zachariah, M. R.: Combined on-line differential mobility and particle mass analysis for determination of size resolved particle density and microstructure evolution, Microporous Mesoporous Mater., 153, 210–216, doi:10.1016/j.micromeso.2011.11.017, 2012.

Lohmann, U. and Feichter, J.: Global indirect aerosol effects: a review, Atmos. Chem. Phys., 5, 715–737, doi:10.5194/acp-5-715-2005, 2005.

Mackay, J. and Mensah, G. A.: Atlas of heart disease and stroke, World Health Organization (WHO), Geneva, 2004.

McCormick, R. A. and Ludwig, J. H.: Climate modification by atmospheric aerosols, Science, 156, 1358–1359, 1976.

McFiggans, G., Artaxo, P., Baltensperger, U., Coe, H., Facchini, M. C., Feingold, G., Fuzzi, S., Gysel, M., Laaksonen, A., Lohmann, U., Mentel, T. F., Murphy, D. M., O'Dowd, C. D., Snider, J. R., and Weingartner, E.: The effect of physical and chemical aerosol properties on warm cloud droplet activation, Atmos. Chem. Phys., 6, 2593–2649, doi:10.5194/acp-6-2593-2006, 2006.

McMurry, P. H., Wang, X., Park, K., and Ehara, K.: The relationship between mass and mobility foratmospheric particles: a new technique for measuring particle density, Aerosol Sci. Tech., 36, 227–238, doi:10.1080/027868202753504083, 2002.

Mikhailov, E., Vlasenko, S., Niessner, R., and Pöschl, U.: Interaction of aerosol particles composed of protein and saltswith water vapor: hygroscopic growth and microstructural rearrangement, Atmos. Chem. Phys., 4, 323–350, doi:10.5194/acp-4-323-2004, 2004.

ACPD
14, 23161–23200, 2014

Moore, R. H., Nenes, A., and Medina, J.: Scanning mobility CCN analysis – a method for fast measurements of size-resolved CCN distributions and activation kinetics, Aerosol Sci. Tech., 44, 861–871, doi:10.1080/02786826.2010.498715, 2010.

Park, K., Cao, F., Kittelson, D. B., and McMurry, P. H.: Relationship between particle mass and mobility for diesel exhaust particles., Environ. Sci. Technol., 37, 577–583, 2003a.

Park, K., Kittelson, D. B., and McMurry, P. H.: A closure study of aerosol mass concentration measurements: comparison of values obtained with filters and by direct measurements of mass distributions, Atmos. Environ., 37, 1223–1230, doi:10.1016/S1352-2310(02)01016-6, 2003b.

Petters, M. D. and Kreidenweis, S. M.: A single parameter representation of hygroscopic growth and cloud condensation nucleus activity, Atmos. Chem. Phys., 7, 1961–1971, doi:10.5194/acp-7-1961-2007, 2007.

Pope III, C. A. and Dockery, D. W.: Health effects of fine particulate air pollution?: lines that connect, J. Air Waste Manage. Assoc., 56, 709–742, 2006.

Pope III, C. A., Ezzati, M., and Dockery, D. W.: Fine-particulate air pollution and life expectancy in the United States, N. Engl. J. Med., 360, 376–386, doi:10.1056/NEJMsa0805646, 2009.

Ramanathan, V., Crutzen, P. J., Kiehl, J. T., and Rosenfeld, D.: Aerosols, climate, and the hydrological cycle, Science, 294, 2119–2124, doi:10.1126/science.1064034, 2001.

Roberts, G. and Nenes, A.: A continuous-flow streamwise thermal-gradient CCN chamber for atmospheric measurements, Aerosol Sci. Tech., 39, 206–221, doi:10.1080/027868290913988, 2005.

Rosenorn, T., Kiss, G., and Bilde, M.: Cloud droplet activation of saccharides and levoglucosan particles, Atmos. Environ., 40, 1794–1802, doi:10.1016/j.atmosenv.2005.11.024, 2006.

Ruehl, C. R., Chuang, P. Y., and Nenes, A.: Aerosol hygroscopicity at high (99 to 100 %) relative humidities, Atmos. Chem. Phys., 10, 1329–1344, doi:10.5194/acp-10-1329-2010, 2010.

Saathoff, H., Naumann, K.-H., Schnaiter, M., Schöck, W., Möhler, O., Schurath, U., Weingartner, E., Gysel, M., and Baltensperger, U.: Coating of soot and $(NH_4)_2SO_4$ particles by ozonolysis products of α-pinene, J. Aerosol Sci., 34, 1297–1321, doi:10.1016/S0021-8502(03)00364-1, 2003.

Scheckman, J. H., McMurry, P. H., and Pratsinis, S. E.: Rapid characterization of agglomerate aerosols by in situ mass-mobility measurements, Langmuir, 25, 8248–8254, doi:10.1021/la900441e, 2009.

ACPD
14, 23161–23200, 2014

Shiraiwa, M., Ammann, M., Koop, T., and Pöschl, U.: Gas uptake and chemical aging of semisolid organic aerosol particles, P. Natl. Acad. Sci. USA, 108, 11003–11008, doi:10.1073/pnas.1103045108, 2011.

Skillas, G., Kunzel, S., Burtscher, H., Baltensperger, U., and Siegmann, K.: High fractal-like dimension of diesel soot agglomorates, J. Aerosol Sci., 29, 411–419, 1998.

Skillas, G., Burtscher, H., Siegmann, K., and Baltensperger, U.: Density and fractal-like dimension of particles from a laminar diffusion flame., J. Colloid Interface Sci., 217, 269–274, doi:10.1006/jcis.1999.6370, 1999.

Sorjamaa, R. and Laaksonen, A.: The effect of H_2O adsorption on cloud drop activation of insoluble particles: a theoretical framework, Atmos. Chem. Phys., 7, 6175–6180, doi:10.5194/acp-7-6175-2007, 2007.

Stratmann, F., Bilde, M., Dusek, U., Frank, G. P., Hennig, T., Henning, S., Kiendler-Scharr, A., Kiselev, A., Kristensson, A., Lieberwirth, I., Mentel, T. F., Pöschl, U., Rose, D., Schneider, J., Snider, J. R., Tillmann, R., Walter, S., and Wex, H.: Examination of laboratory-generated coated soot particles: an overview of the LACIS Experiment in November (LExNo) campaign, J. Geophys. Res., 115, D11203, doi:10.1029/2009JD012628, 2010.

Sugio, S., Kashima, A., Mochizuki, S., Noda, M., and Kobayashi, K.: Crystal structure of human serum albumin at 2.5 A resolution, Protein Eng., 12, 439–446, 1999.

Tranfield, E. M. and Walker, D. C.: Understanding of human illness and death following exposure to particulate matter air pollution, in: Environmental Health – Emerging Issues and Practice, edited by: J. Oosthuizen, InTech, Rijeka, Croatia, 81–102, 2012.

Twomey, A., Piepgrass, M., and Wolfe, T. L.: An assessment of the impact of pollution on global cloud albedo, Tellus B, 36, 356–366, 1984.

Twomey, S.: Pollution and the planetary albedo, Atmos. Environ., 8, 1251–1256, 1974.

Virtanen, A., Ristimäki, J., and Keskinen, J.: Method for measuring effective density and fractal dimension of aerosol agglomerates, Aerosol Sci. Tech., 38, 437–446, doi:10.1080/02786820490445155, 2004.

ACPD
14, 23161–23200, 2014

Table 1. Thermodynamic properties of components used in this study.

	Molar mass ($g\,mol^{-1}$)	Density ($g\,cm^{-3}$)	Solubility in water (Mass %)	κ
$(NH_4)_2SO_4$	132.14[a]	1.77[a]	43.3[a]	0.61[e]
Sucrose	342.3[a]	1.58[a]	67.1[a]	0.084[f]
BSA	66 500[b]	1.362[b]	60[d]	0.013[g]
SiO_2	60.08[a]	2.16[c]	–	–

[a] Haynes et al. (2013)
[b] Mikhailov et al. (2004)
[c] Grayson (1985)
[d] Shiraiwa et al. (2011)
[e] Petters and Kreidenweis (2007)
[f] Ruehl et al. (2010)
[g] This work.

ACPD
14, 23161–23200, 2014

Table 2. The total soluble fraction of the solute masses in the bulk mixtures, the fraction of total soluble mass mixed with silica, the average soluble mass fraction of the mixed particles (calculated from particle size distributions, see text for details).

Soluble mass fraction in the bulk mixture (%)	Fraction of total soluble mass mixed with silica (%)			Total soluble mass fraction in the mixed particles (%)		
	Silica + $(NH_4)_2SO_4$	Silica + sucrose	Silica + BSA	Silica + $(NH_4)_2SO_4$	Silica + sucrose	Silica + BSA
25	92	98	87	23.4	24.6	22.5
10	88	99	99	8.9	9.9	9.9
5	87	99	~ 100	4.4	4.9	~ 5

ACPD
14, 23161–23200, 2014

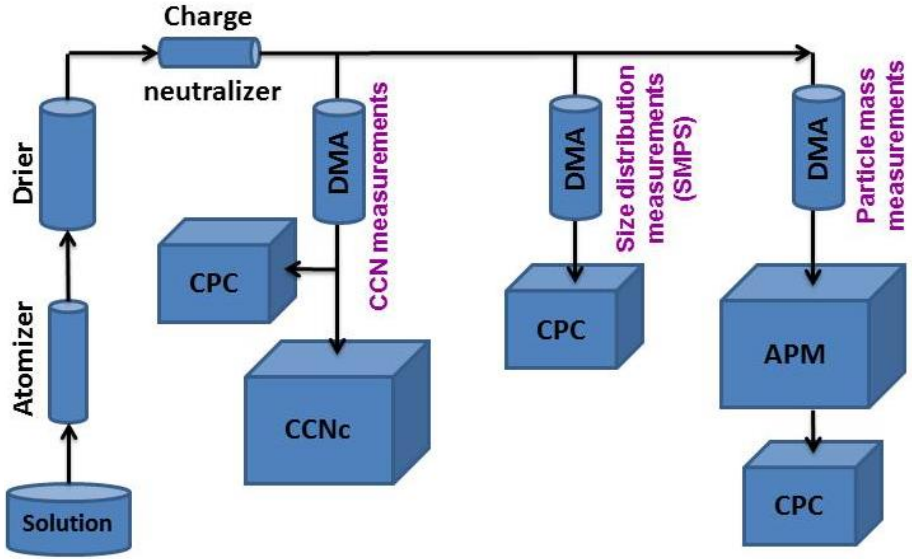

Figure 1. Schematic of the experimental set up and three types of measurements: CCN activity measurements, size distribution measurements by SMPS and particle mass analyzing by APM.

ACPD
14, 23161–23200, 2014

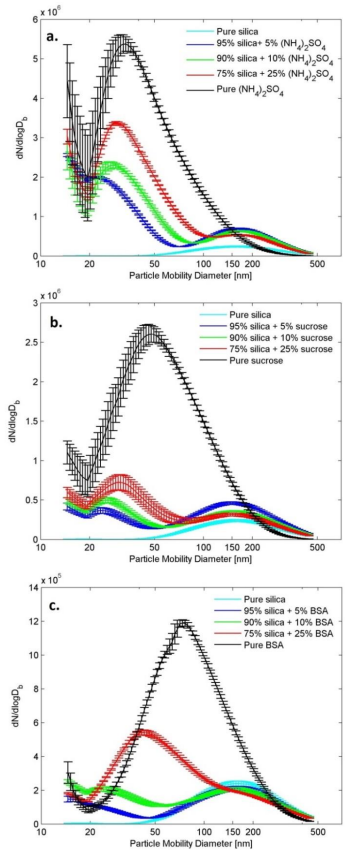

Figure 2. Average particle number size distributions (SMPS) for silica particles mixed with **(a)** $(NH_4)_2SO_4$, **(b)** sucrose and **(c)** BSA. Each average size distribution is based on at least 70 individual size distributions, and the error bars represent the standard deviation of the measurements.

ACPD
14, 23161–23200, 2014

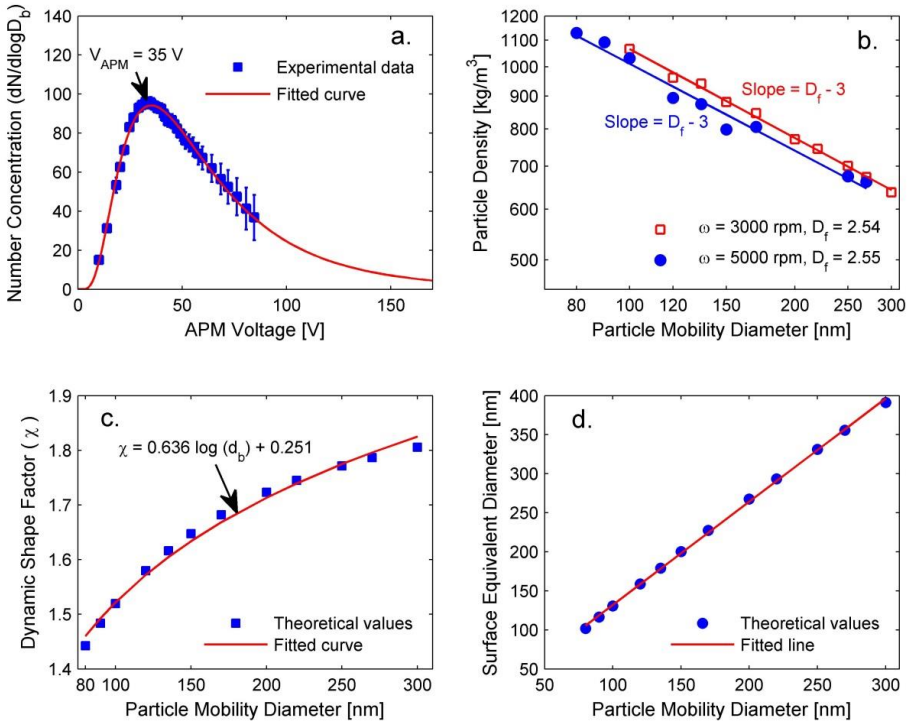

Figure 3. (a) Average number concentration of 100 nm (mobility size) pure silica particles downstream the APM and at a rotation speed of the APM of 3000 rpm. The number concentrations were averaged over one minute for each APM voltage, and the error bars represent the standard deviation of about 60 measurements recorded under the same conditions. **(b)** Density of silica particles for different mobility diameters and two different rotation speeds of the APM (3000 and 5000 rpm). The fitted fractal dimensions are 2.54 and 2.55, respectively. **(c)** Dynamic shape factor vs. electrical mobility diameter for silica particles, **(d)** Theoretical surface equivalent diameter against mobility diameter of the silica particles.

ACPD
14, 23161–23200, 2014

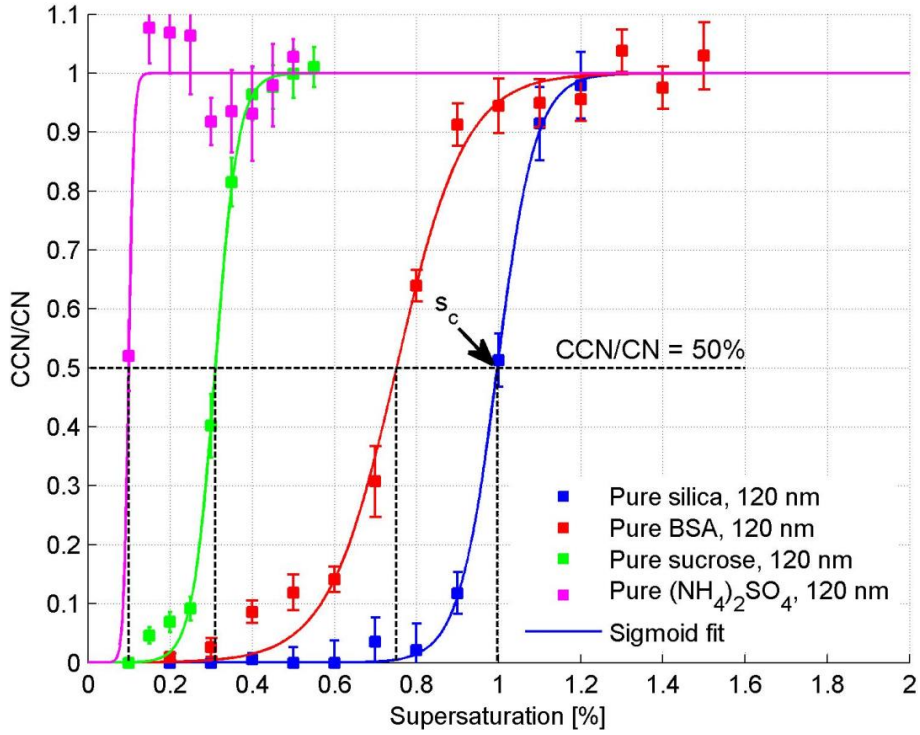

Figure 4. The average activation ratio of pure soluble or insoluble particles with the mobility diameter of 120 nm at different supersaturations. Error bars represent the standard deviation of the activation efficiency of about 20 measurements corresponding to each supersaturation of the instrument. Critical supersaturation s_c is defined as the point where the activation ratio is equal to 50 %.

ACPD
14, 23161–23200, 2014

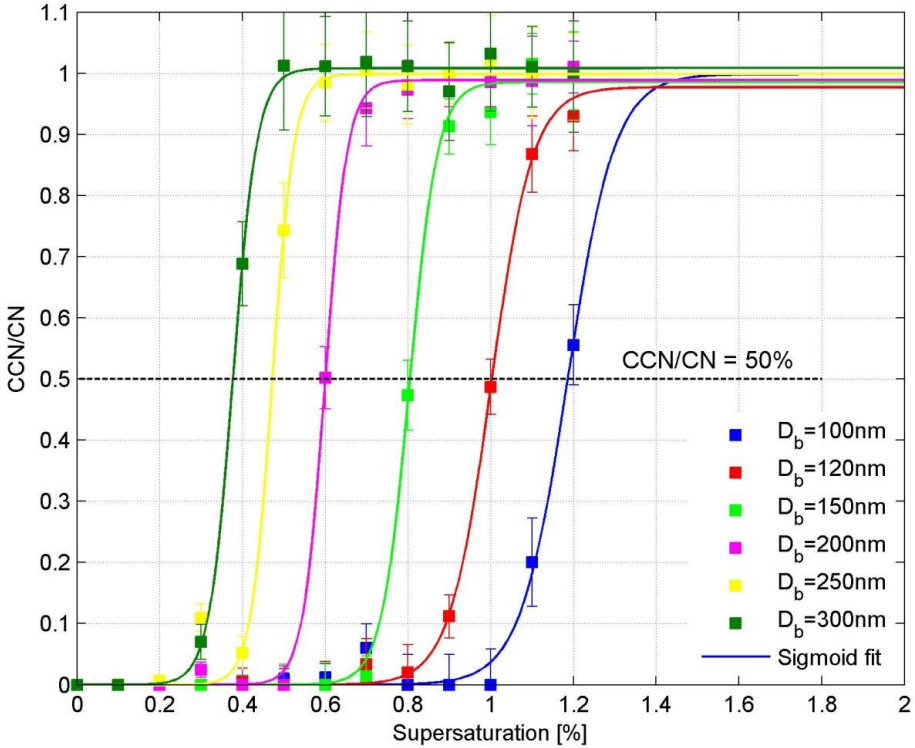

Figure 5. The average activation ratio vs. supersaturation for different mobility diameters of silica particles. Error bars represent the standard deviation of the measured activation efficiency as a result of about 20 measurements corresponding to each supersaturation of the instrument.

ACPD
14, 23161–23200, 2014

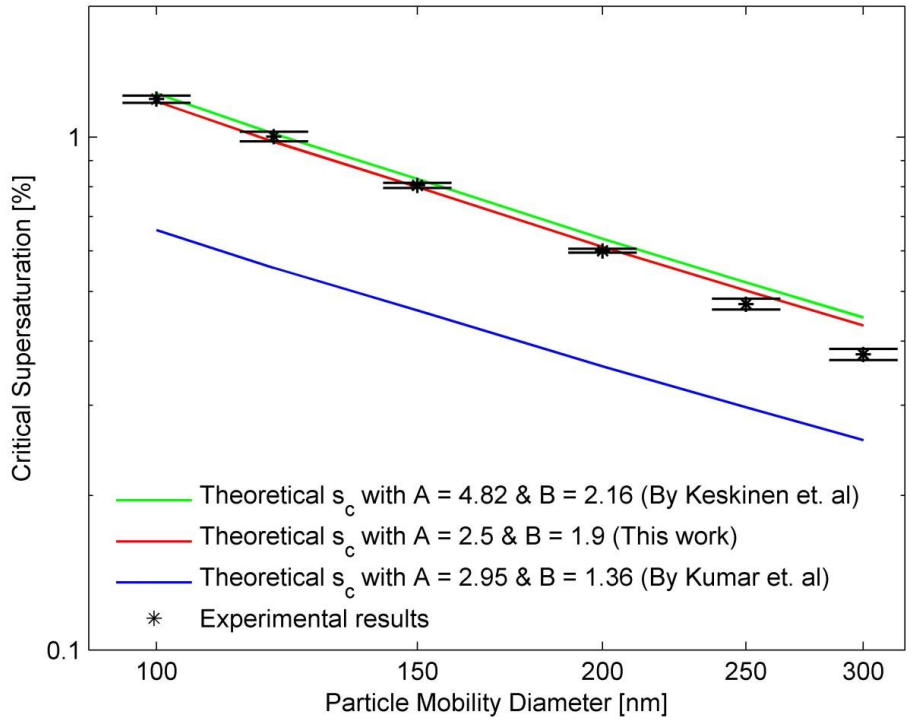

Figure 6. Critical supersaturations against activation mobility diameter of pure silica particles with different FHH adsorption isotherm parameters from different studies compared to experimental results. Error bars represent the minimum vs. maximum values of supersaturation to estimate the s_c corresponding to each d_b.

ACPD
14, 23161–23200, 2014

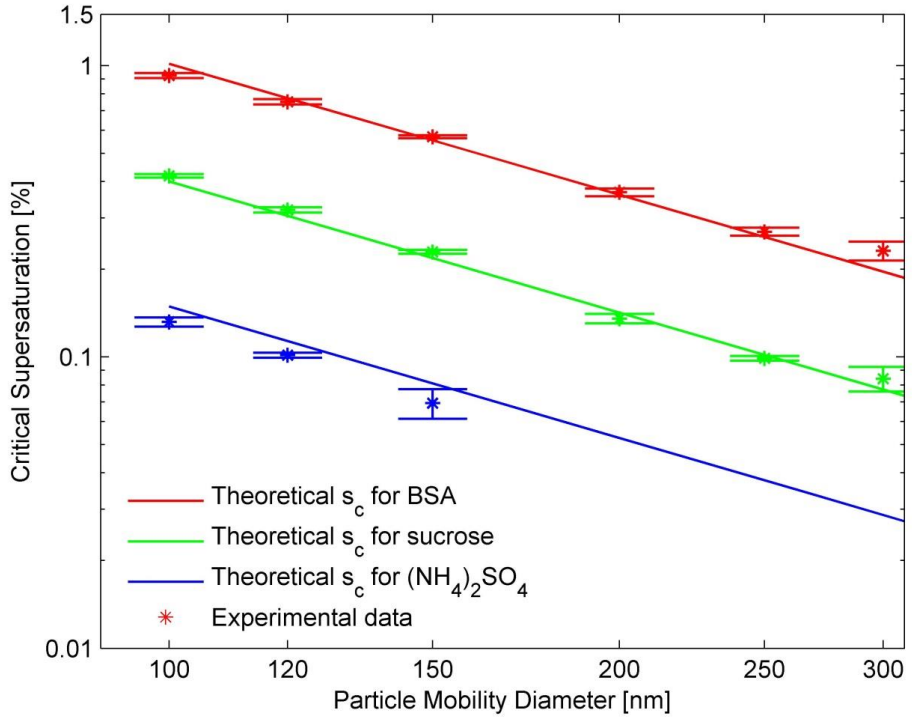

Figure 7. Experimental and theoretical critical supersaturations of pure $(NH_4)_2SO_4$, sucrose and BSA particles for different mobility diameters based on κ-Köhler theory. Error bars represent the minimum vs. maximum values of supersaturation to estimate the s_c corresponding to each d_b.

ACPD
14, 23161–23200, 2014

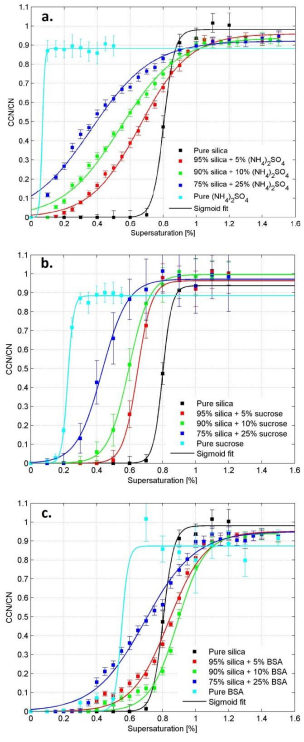

Figure 8. (a) Activation ratio curves for different supersaturations of silica + $(NH_4)_2SO_4$ particles of 150 nm mobility diameter, **(b)** activation ratio curves for different supersaturations of silica + sucrose particles of 150 nm mobility diameter, **(c)** activation ratio curves for different supersaturations of silica + BSA particles of 150 nm mobility diameter. Error bars represent the standard deviation of the measured activation efficiency as a result of about 20 measurements corresponding to each supersaturation of the instrument.

ACPD
14, 23161–23200, 2014

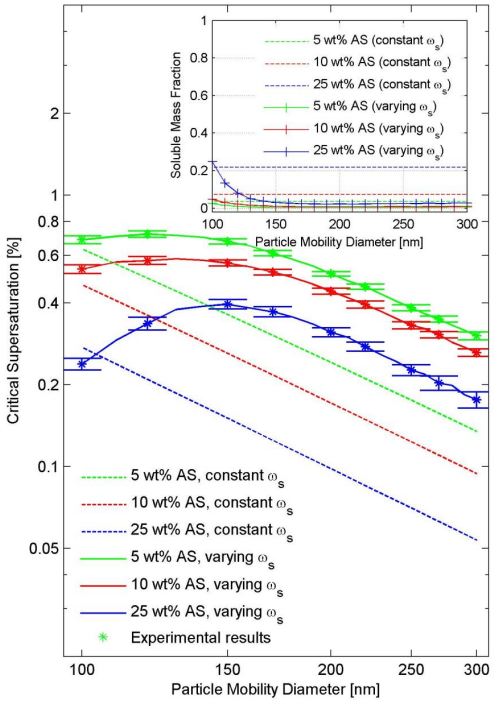

Figure 9. Experimental and theoretical critical supersaturations for mixed silica + $(NH_4)_2SO_4$ (AS) particles for different particle mobility diameters using shell-and-core model. Dashed lines represent calculated critical supersaturations based on an assumption of constant soluble mass fractions (ω_s) with changing diameter and solid lines show the critical supersaturations based on the size-dependent soluble mass fractions. Error bars represent the minimum vs. maximum values of supersaturation to estimate the s_c corresponding to each mobility diameter. The insert represents assumed constant soluble mass fractions as well as size-dependent ones corresponding to the 50 % points in the CCN/CN curves for different size vs. supersaturation pairs of mixed silica + $(NH_4)_2SO_4$ particles.

ACPD
14, 23161–23200, 2014

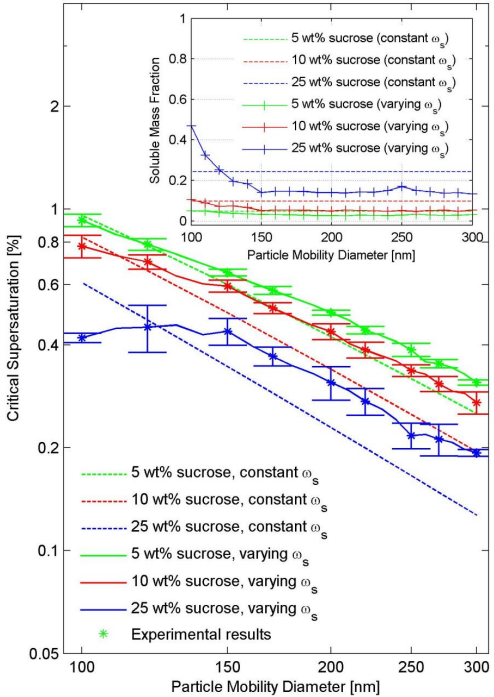

Figure 10. Experimental and theoretical critical supersaturations for mixed silica + sucrose particles for different particle mobility diameters using shell-and-core model. Dashed lines represent calculated critical supersaturations based on an assumption of constant soluble mass fractions (ω_s) with changing diameter and solid lines show the critical supersaturations based on the size-dependent soluble mass fractions. Error bars represent the minimum vs. maximum values of supersaturation to estimate the s_c corresponding to each mobility diameter. The insert represents assumed constant soluble mass fractions as well as size-dependent ones corresponding to the 50 % points in the CCN/CN curves for different size vs. supersaturation pairs of mixed silica + sucrose particles.

ACPD
14, 23161–23200, 2014

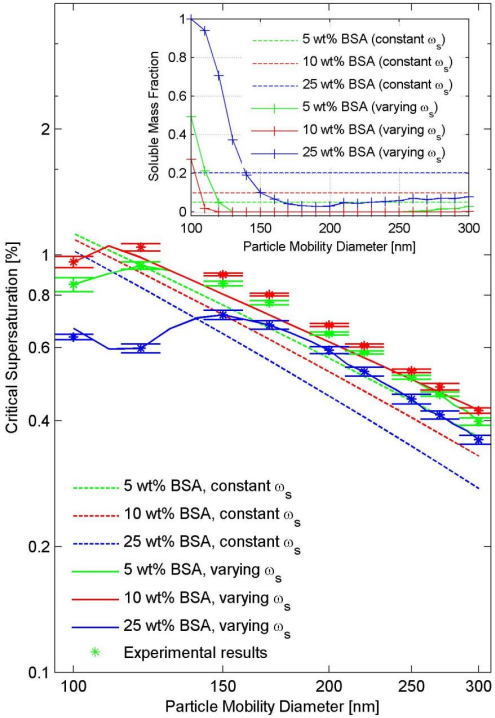

Figure 11. Experimental and theoretical critical supersaturations for mixed silica + BSA particles for different particle mobility diameters using shell-and-core model. Dashed lines represent calculated critical supersaturations based on an assumption of constant soluble mass fractions (ω_s) with changing diameter and solid lines show the critical supersaturations based on the size-dependent soluble mass fractions. Error bars represent the minimum vs. maximum values of supersaturation to estimate the s_c corresponding to each mobility diameter. The insert represents assumed constant soluble mass fractions as well as size-dependent ones corresponding to the 50 % points in the CCN/CN curves for different size vs. supersaturation pairs of mixed silica + BSA particles.

ACPD
14, 23161–23200, 2014

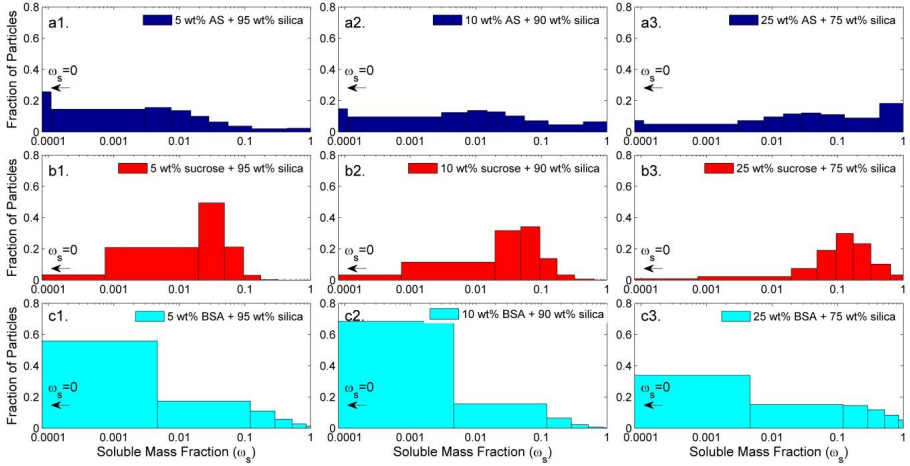

Figure 12. The distribution of soluble material on 150 nm (mobility diameter) particles in the mixed particles made of **(a1–3)** silica + $(NH_4)_2SO_4$ (AS), **(b1–3)** silica + sucrose, **(c1–3)** silica + BSA. Note that the smallest solubility bin extends down to zero, i.e. particles consisting of pure silica.

ACPD
14, 23161–23200, 2014